Materials Science & Engineering A 736 (2018) 156–166

Contents lists available at ScienceDirect

Materials Science & Engineering A

journal homepage: www.elsevier.com/locate/msea

Strong resistance to hydrogen embrittlement of high-entropy alloy

Z. Pu[a,b], Y. Chen[a,b,*], L.H. Dai[a,b,c,*]

[a] State Key Laboratory of Nonlinear Mechanics, Institute of Mechanics, Chinese Academy of Sciences, Beijing 100190, People's Republic of China
[b] School of Engineering Science, University of Chinese Academy of Sciences, Beijing 101408, People's Republic of China
[c] State Key Laboratory of Explosion Science and Technology, Beijing Institute of Technology, Beijing 100081, People's Republic of China

ARTICLE INFO

Keywords:
High-entropy alloy
Hydrogen embrittlement
Cryogenic temperature
Ductility
Deformation microstructure

ABSTRACT

The resistance to hydrogen embrittlement (HE) of CrMnFeCoNi high-entropy alloy (HEA) at both room and cryogenic temperatures was examined through tensile experiments on specimens hydrogenated via cathodic electrochemical charging method. Two representative steels, i.e. 316L stainless steel (SS) and X80 pipeline steel (PS), were chosen for comparison due to their similar main constituent elements to CrMnFeCoNi HEA. Results show that the hydrogen pre-charged CrMnFeCoNi HEA has the smallest loss of ductility among the three materials at room temperature, while displays no reduction of elongation at 77 K, compared with the uncharged one. Fracture surfaces at both room and cryogenic temperatures of hydrogen pre-charged CrMnFeCoNi HEA are mainly composed of dimples, indicating ductile fractures, while brittle characteristics occur in pre-charged 316L SS and X80 PS. Typical deformation microstructure of the hydrogen pre-charged CrMnFeCoNi HEA at room temperature is tangled dislocations instead of highly dense dislocation walls (HDDWs) found in the pre-charged 316L SS. At 77 K, more deformation twins are formed in the both materials. Reasons for a higher resistance to HE of CrMnFeCoNi HEA at room temperature are attributed to the formation of less hydrogen trapping sites, thus a lower degree of hydrogen enrichment than 316L SS. While at 77 K, the atomic hydrogen is not able to promptly accumulate near these trapping sites due to its slow diffusion rate, which leads to strong HE resistance.

1. Introduction

The emergence of high-entropy alloys (HEAs) has significantly widened the idea of material design and provided new challenges to material scientists. Different from traditional alloys in which usually one or two dominant elemental components are present, HEAs are a unique class of alloys that contain multiple principal elements in equimolar or near-equimolar ratios [1,2]. First introduced about a decade back [3,4], HEAs have attracted increasing research attentions due to their excellent mechanical performance, such as good strength-ductility combinations [5,6], exceptional strengthening effect [7], excellent fracture toughness at cryogenic temperature [8] and encouraging fatigue resistance [9]. However, future structural components made of HEAs are likely to be exposed in some special working environment of a number of potential applications. Some such examples are welding process [10], nuclear power plants [11], or humid environment industry [12], where the concentration of hydrogen is relatively high. Since hydrogen can cause catastrophic damages to a variety of metallic materials [13–18], it is essential to consider the interaction of HEAs with hydrogen and investigate the ability of resistance to hydrogen embrittlement (HE) of the HEAs.

It was reported that hydrogen deteriorates the mechanical behavior of steel materials as early as 1874 [19]. Since then the HE problems multiplied and various researches have been devoted to the exploration of the mechanisms of HE [17,18,20–28]. Hydrogen reduces the service life of metallic materials in several different ways, leading to a decrease in their capability for plastic deformation or even a loss in strength [29,30]. The main influence factors on the degree of HE are hydrogen solubility and diffusivity [24,31], temperature [32], deformation mechanism [30,33] and alloying effect [34,35]. Although the underlying atomic processes of how hydrogen interacts with materials and lead to their embrittlement remain controversial, four main mechanisms for HE have been proposed: (1) Formation of a hydride phase; (2) Formation of hydrogen bubbles; (3) Hydrogen-enhanced localized plasticity (HELP); (4) Hydrogen-enhanced decohesion (HEDE). In general, the hydride phase occurs only in alloys with transitional metallic elements that have strong hydrogen affinity such as zirconium, titanium or other transition [28]. The theory of hydrogen bubbles suggests that once the cavities that occupied by high concentration of hydrogen grow to a critical size, the internal gas pressure can be sufficient to mechanical blister the

* Corresponding authors at: State Key Laboratory of Nonlinear Mechanics, Institute of Mechanics, Chinese Academy of Sciences, Beijing 100190, People's Republic of China.
E-mail addresses: chenyan@lnm.imech.ac.cn (Y. Chen), lhdai@lnm.imech.ac.cn (L.H. Dai).

https://doi.org/10.1016/j.msea.2018.08.101
Received 25 July 2018; Received in revised form 22 August 2018; Accepted 28 August 2018
Available online 04 September 2018
0921-5093/

material [22]. Based on experimental observations [20,36,37] and theoretical calculations [38–40], the HELP theory claims that by shielding the elastic interactions between dislocations and elastic centers, the solute hydrogen enhances dislocation velocities which can lead to localized stress and deformation [31,41,42]. As a result, fracture occurs in the vicinity of these localized zones. On the other hand, the HEDE theory suggests that high density of trapping sites is produced during the deformation of materials and the filling of these sites with hydrogen leads to embrittlement by reducing the lattice cohesion [23,25,33,43,44]. In view of the complexity of HE problems and the safety for future hydrogen related engineering, exploring a material with strong resistance to HE and revealing its intrinsic mechanisms is of great importance. For HE problems in HEA, it has been reported that the HEA has a reduced susceptibility to HE under gaseous hydrogen charging condition [45,46] and the pre-strain does not affect its excellent HE resistance [47]. By cryogenic temperature caliber rolling, an HEA with remarkably high tensile strength shows great resistance to HE [48] and a joint increase in both strength and ductility is feasible in HEA with a proper hydrogen concentration [49]. Besides, the HE resistance in a classical HEA with varying composition was also investigated [50,51]. It shows that HEA may be a good candidate for HE resistance, however, the performance and mechanism of HE in HEA are still far from being fully understood.

In this study, we choose a classical type of HEA, CrMnFeCoNi, which has extremely stable single FCC structure, high fracture toughness and an excellent combination of strength and ductility, as discussed in early studies [5,8]. The tensile properties of CrMnFeCoNi HEA with and without hydrogen charging are investigated at room temperature and liquid nitrogen temperature (77 K). For comparison, the same experiments were also carried out on two traditional steels that have the similar main constituent elements, which are 316L stainless steel (SS) and X80 pipeline steel (PS), respectively. It shows that the CrMnFeCoNi HEA has the strongest resistance to HE among these three materials at room temperature and liquid nitrogen temperature (77 K). Based on fracture mode and deformation microstructure analysis of the three materials, the fundamental mechanisms for a higher HE resistance in HEA are revealed.

2. Experimental methods

2.1. Materials processing

The HEA used in this study was processed by arc-melting a mixture of pure metals with a nominal composition $Cr_{20}Mn_{20}Fe_{20}Co_{20}Ni_{20}$ (at %) in a high purity argon atmosphere. The ingot was remelted at least five times to ensure homogeneity before it was drop-cast into a rectangular-cross-section copper mould. The as-cast ingot was cold rolled by 70% reduction in thickness.

Recrystallization at 820 °C for 1 h resulted in an equiaxed grain structure with an average grain size of 8 μm (Fig. 1a). Tensile specimens were sliced from the recrystallized sheet, ground with SiC papers on each side, resulting in a final specimen thickness of 1.2 mm and a gauge section width of 2.5 mm. The crystal structure was identified by X-ray diffraction (XRD) to be a single FCC phase (Fig. 2). The average grain sizes of 316L SS and X80 PS are 20 μm and 60 μm, as shown in Fig. 1b and c, respectively. Besides, plenty of rectangular annealing twins can be found in the CrMnFeCoNi HEA and 316L SS (Fig. 1a and b). The chemical compositions of the three materials are shown in Table 1.

2.2. Hydrogenation method

Hydrogen was introduced into the tensile specimens using a cathodic electrochemical charging technique in a 0.5 mol/L H_2SO_4 + 1 g/L CH_4N_2S (thiourea) solution with constant current density of 20 mA/cm^2 at room temperature. The hydrogenation time was chosen to be 18 h, after which the effect of hydrogen on the performance of the tensile specimens has become apparent. Besides, a diffusible hydrogen analyzer (BRUKER, G4 PHOENIX) was used to measure the hydrogen content of the three materials immediately after the hydrogenation process.

2.3. Mechanical testing

Tensile tests were performed at an engineering strain rate of 10^{-3} s^{-1} in a MTS-CMT5105S with a low temperature environmental chamber. The three types of materials with and without hydrogen charging were tensioned at room temperature and liquid nitrogen temperature (77 K). For each case, three identical specimens were tested to guarantee the repeatability. To ensure that the hydrogen does not escape from the sample because of diffusion, tensile test was performed forthwith after the hydrogen charging.

2.4. Microstructure characterization

To uncover micro-deformation mechanisms, the fracture surfaces of the three materials were carefully observed by a scanning electron microscope (SEM, JEOL, JSM-7100F). Furthermore, transmission electron microscope (TEM, JEOL, JEM-2100F) was used to characterize the deformation microstructures that are related to HE, such as fine dislocations, stacking faults or mechanical twins. To ensure that the TEM study was carried out on the hydrogen affected zone, of which the depth is relatively shallow when using electrochemical charging method [31,45], discs with a diameter of 3 mm were cut from the slices near the surface of the gauge sections.

3. Results and discussion

3.1. Hydrogen content and affected zone

The content of hydrogen introduced during the hydrogenation process of the three materials is shown in Table 2. As a result, the hydrogen content of CrMnFeCoNi HEA is almost the same as that of 316L SS, but obviously higher than that of X80 PS. It is reasonable to speculate that the dissolved hydrogen in this X80 PS, a ferritic steel, has reached saturation, since the ferrite generally has larger diffusivity but smaller lattice solubility of hydrogen than austenite [31].

The HE affected zone can be described by hydrogen diffusion depth through lattice, L [52], which is calculated by the following equations:

$$L = \sqrt{2D_H t} \tag{1}$$

$$D_H = D_0 \exp(-\frac{Q}{RT}) \tag{2}$$

where D_0 and D_H are the pre-exponential coefficient and hydrogen diffusivity, respectively, t is the hydrogen charging time, Q is the activation energy of hydrogen diffusion, R is the gas constant and T is the temperature during the charging process (here we take T to 300 K). We assume that the parameters to calculate the diffusion coefficient D_H of HEA are similar to those of austenitic SS, since they both have the same crystal structure (fcc) and main chemical constituents [53]. Besides, D_H of austenitic SS is reported to be nearly insensitive to the composition [54]. Therefore, adopting $D_0 = 6.2 \times 10^{-7}$ m^{2}s^{-1} and $Q = 53.6$ kJ mol^{-1} from austenitic SS [55] and $D_0 = 2.0 \times 10^{-7}$ m^{2}s^{-1} and $Q = 6.87$ kJ mol^{-1} from α-Fe [56], L is estimated to be 10 μm for CrMnFeCoNi HEA and 316L SS and 57.6 cm for X80 PS. This result indicates that the hydrogen can penetrate the X80 PS during the hydrogenation process while it can only affect the other two FCC materials in a shallow depth.

3.2. Tensile properties

Representative engineering stress-strain curves of the CrMnFeCoNi HEA, 316L SS and X80 PS tensile tested to fracture at room temperature

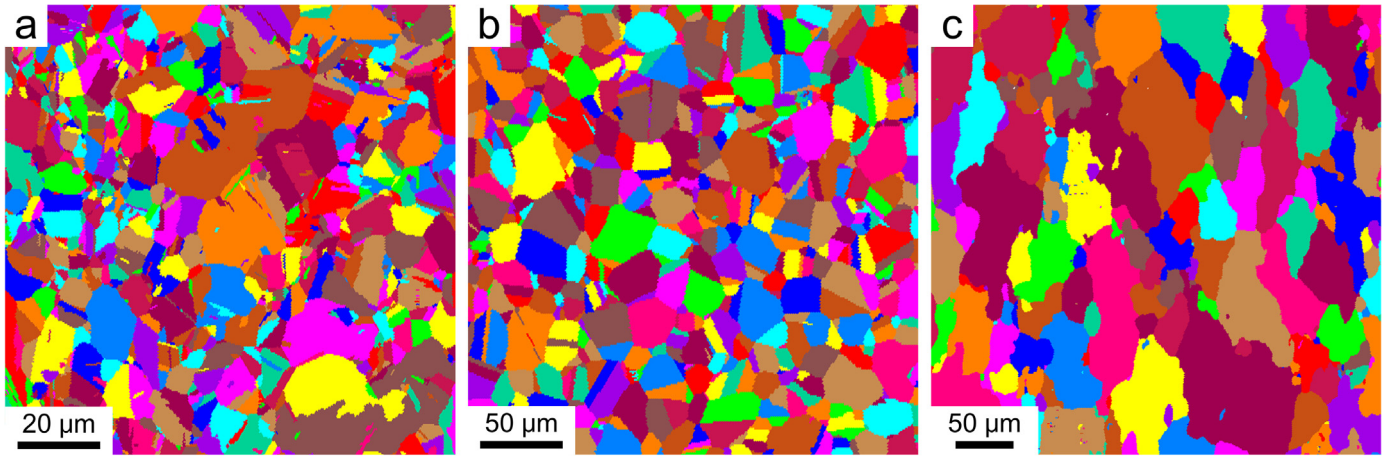

Fig. 1. Representative backscattered electron micrographs of the microstructures of the three materials. (a) CrMnFeCoNi HEA. (b) 316L SS. (c) X80 PS.

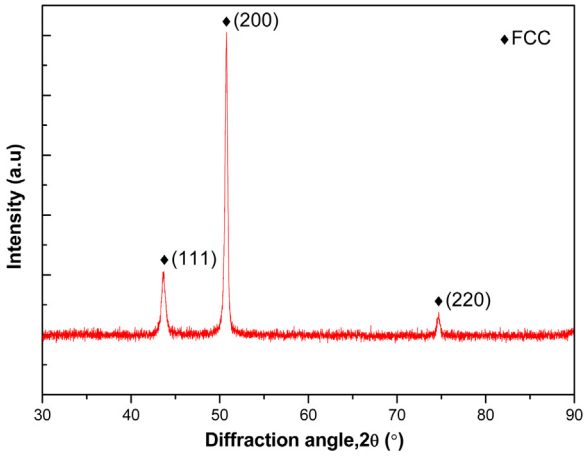

Fig. 2. XRD pattern of the CrMnFeCoNi HEA indicating a single FCC structure.

with and without hydrogen charging are shown in Fig. 3a–c. The results illustrate that the strain to failure ε_f of CrMnFeCoNi HEA reduces from 0.52 to 0.45 after hydrogen charging for 18 h while its yield and tensile strength remain approximately the same (Fig. 3a). For 316L SS, ε_f decreases from 0.74 to 0.55, which is more severe compared to the CrMnFeCoNi HEA albeit its original yield and tensile strength are sustained after hydrogen charging (Fig. 3b). As for X80 PS, both the elongation and tensile strength diminish greatly after hydrogen charging, i.e., from 0.33 to 0.15 and 760–650MPa, respectively (Fig. 3c). The HE susceptibility of materials is commonly measured by a value I_{HE}, which is the relative loss of ductility or strength, and the smaller the value, the lower the susceptibility of the material [57]. In this article, the susceptibility to HE can be expressed by the percentage loss of tensile strain after hydrogen charging as shown below:

$$I_{HE} = (1 - \varepsilon_{f_H}/\varepsilon_{f_0}) \times 100\% \quad (3)$$

where ε_{f_0} and ε_{f_H} are respectively the strain to failure before and after hydrogen charging. The I_{HE} calculated from Eq. (3) for CrMnFeCoNi HEA, 316L SS and X80 PS are 13%, 25% and 53% (Fig. 3d), respectively, indicating that the CrMnFeCoNi HEA has the lowest susceptibility to HE of the three materials at room temperature.

Table 2
Hydrogen concentration of the three materials after hydrogenation.

Sample types	HEA	316L	X80
Hydrogen content (wt p.p.m.)	7.73	7.29	4.36

Take into consideration that the mechanism of plastic deformation in CrMnFeCoNi HEA at cryogenic temperatures is distinct from that at room temperature [5,8] (e.g. from dislocation glide at room temperature to glide plus twinning at 77 K), the interaction of hydrogen with the HEA during deformation and the degree of HE may also change. Hence, the tensile tests were performed with uncharged and pre-charged specimens for the three materials at 77 K. As depicted in Fig. 4, the hydrogen has almost no influence on the strength or ductility of CrMnFeCoNi HEA or 316L SS at such a low temperature (Fig. 4a, b) while a smaller influence on the elongation of X80 PS in contrast to the case at room temperature, for which the degree of susceptibility to HE reduces from 53% (room temperature) to 27% (77 K), see Fig. 3d and Fig. 4c.

3.3. Fractography

The fracture surfaces at room temperature of the three materials with and without hydrogen charging are presented in Fig. 5. Obvious area reduction of cross section due to necking are found in CrMnFeCoNi HEA and 316L SS, both for the uncharged and pre-charged specimens. There is no significant difference in the macroscopical fracture morphology (Fig. 5a–d) although hydrogen has reduced their ductility. However, the fracture surfaces of X80 PS with and without hydrogen charging are widely divergent (Fig. 5e, f) and it can be seen that, for the pre-charged specimen, the reduction of area is obviously smaller than the uncharged one. In addition, the fracture surface of the pre-charged specimen contains a pit as shown by the red dotted line (Fig. 5f), implying that this region is influenced by hydrogen seriously.

Typical local areas of fracture surfaces at room temperature of the three materials are shown in Fig. 6. Since the hydrogen can not diffuse

Table 1
Nominal chemical compositions (wt%) of CrMnFeCoNi HEA, 316L SS, and X80 PS.

	Cr	Mn	Fe	Co	Ni	C	Si	P	S	Mo
HEA	18.88	19.16	19.81	21.22	20.88					
316L	17.13	1.14	Bal.		10.31	0.02	0.54	0.03	0.0007	2.10
X80	0.035	1.00	Bal.			0.61	0.22	0.013	0.0018	0.005

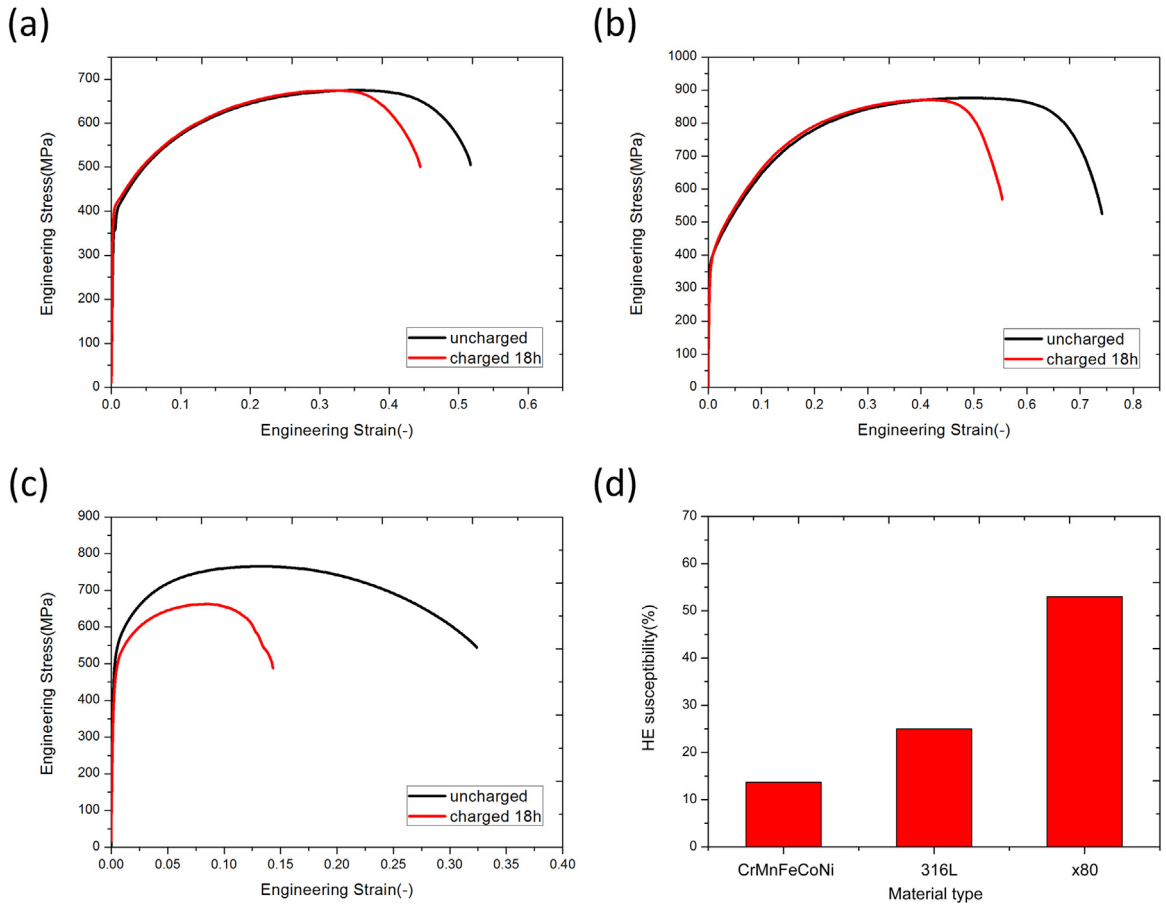

Fig. 3. (a)–(c) Stress-strain curves of CrMnFeCoNi HEA, 316L SS and X80 PS tested at room temperature with and without hydrogen charging. (d) the susceptibility to HE of the three materials.

deeply, these local areas are only from the shallow surfaces of the materials (inside the yellow circles in Fig. 5). The fracture surfaces of CrMnFeCoNi HEA with and without hydrogen charging (Fig. 6a, b) are mainly composed of dimples, and it turns out that the size of these dimples remain almost the same before and after hydrogen charging, indicating that the hydrogen only has little effect on this HEA. For 316L SS, the fracture surface for the uncharged specimen displays more homogeneous dimples (Fig. 6c) compared with CrMnFeCoNi HEA. However, brittle fracture areas are found in the fracture surface of the pre-charged 316L SS (Fig. 6d). These changes of fracture morphology indicate that the influence of hydrogen on 316L SS is more severe than that on the CrMnFeCoNi HEA. Finally, the fracture surfaces of X80 PS with and without hydrogen charging are shown in Fig. 6e and f. It can be found that, the fracture surface is consisted of homogeneous and small dimples in the un-charged specimen (Fig. 6e), but the pre-charged one is mainly composed of sharp tear ridges and facets, which are the features of “quasi-cleavage” (Fig. 6f). It implies that the fracture mode of X80 PS has turned from ductile to brittle in the local region after hydrogen charging for 18 h.

The fracture morphologies for the three materials tested at 77 K with and without hydrogen charging are shown in Fig. 7. It can be found that, the macroscopical cross sections for pre-charged ones show similar traits to those for uncharged ones for all the three materials. It suggests that at cryogenic temperature, the pre-charged hydrogen does not cause obvious change of the fracture mode. Necking is observed in CrMnFeCoNi HEA and 316L SS. However, different from the case at room temperature (Fig. 5e, f), the cross section area of X80 PS at fracture has nearly no reduction at 77 K (Fig. 7e, f), which is a

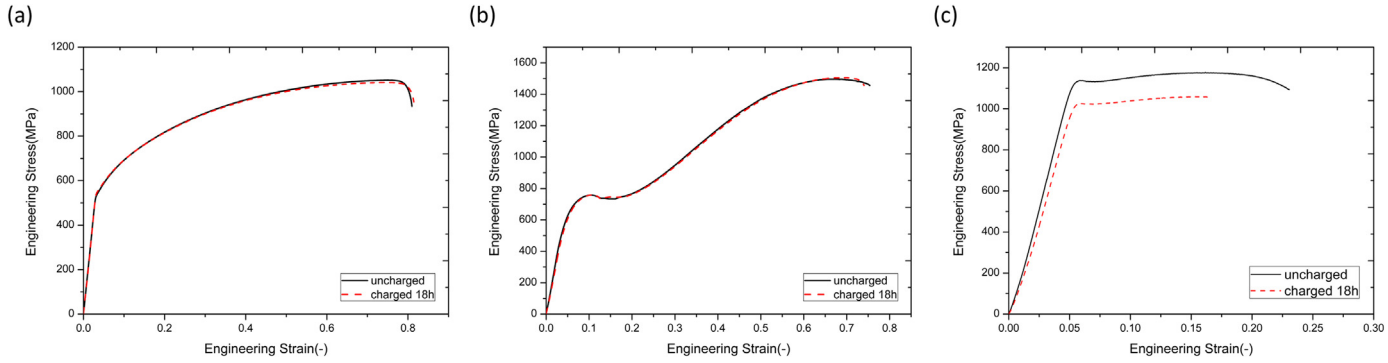

Fig. 4. Stress-strain curves of CrMnFeCoNi HEA, 316L SS and X80 PS tested at 77 K with and without hydrogen charging.

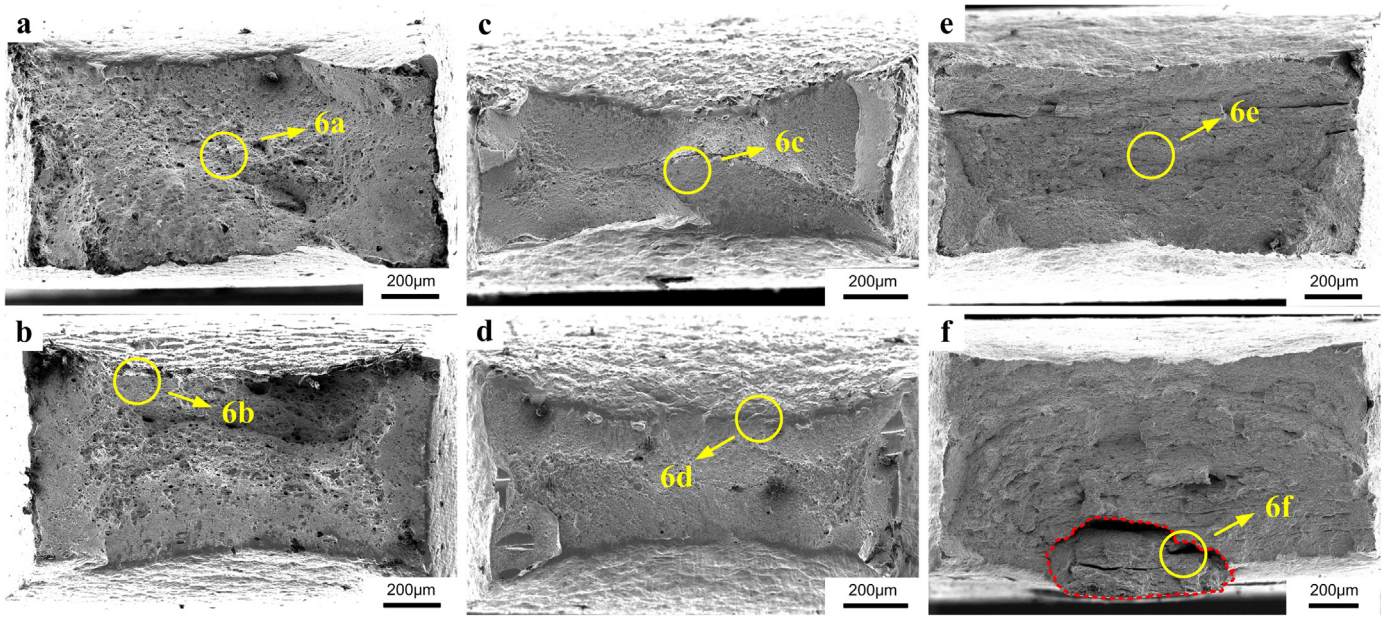

Fig. 5. Fracture morphology of the three materials tested at room temperature with and without hydrogen charging. (a) Uncharged and (b) pre-charged CrMnFeCoNi HEA, (c) uncharged and (d) pre-charged 316L SS and (e) uncharged and (f) pre-charged X80 PS (For interpretation of the references to color in this figure, the reader is referred to the web version of this article.).

manifestation of low ductility.

Fig. 8 is the typical local area (inside the yellow circles in Fig. 7) of fracture surfaces of the three materials tested at 77 K with and without hydrogen charging. Compared with the result at room temperature (Fig. 6a–d), the difference between the fracture patterns of uncharged and pre-charged specimens are minor for both the CrMnFeCoNi HEA and 316L SS (Fig. 8a–d), which shows that the two materials are less affected by hydrogen at low temperature. As for X80 PS, the fracture pattern has changed from dimple (Fig. 6e) at room temperature to cleavage fracture pattern at 77 K (Fig. 8e, f). In addition, much more microcracks can be found in hydrogen pre-charged X80 PS specimen (Fig. 8f) in contrast to the uncharged one (Fig. 8e), since the crack growth ratio can be increased if the hydrogen pressure is enough [58].

3.4. Stress induced hydrogen diffusion

Since the atomic hydrogen dissolved in the pre-charged specimens can get enrichment by diffusion under applied stress and the cracks may nucleate when local hydrogen content exceed the threshold level. Hence, it is very important to estimate the hydrogen diffusion distance L under applied stress in the tensile test for the pre-charged specimens.

Due to the existence of the applied stress, Eq. (2) that calculates the hydrogen diffusivity D_H can be modified to:

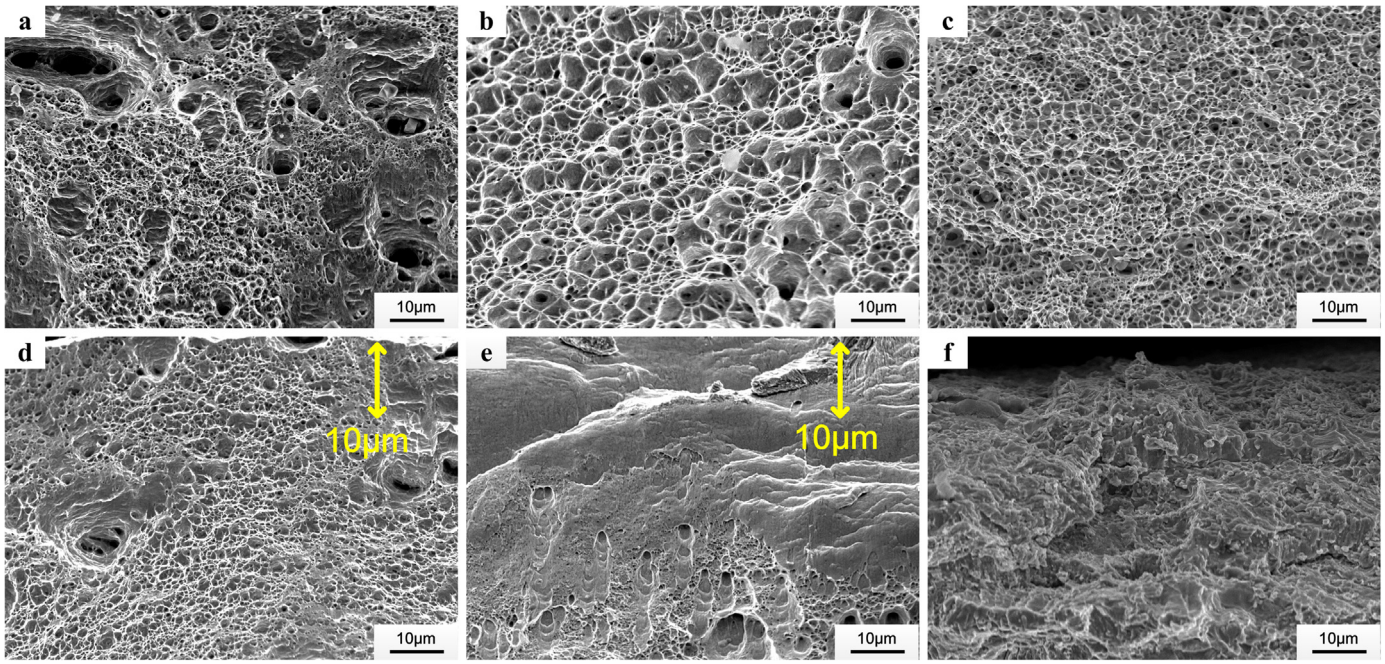

Fig. 6. Typical local area of fracture surfaces of the three materials tested at room temperature with and without hydrogen charging. (a) Uncharged and (b) pre-charged CrMnFeCoNi HEA, (c) uncharged and (d) pre-charged 316L SS and (e) uncharged and (f) pre-charged X80 PS.

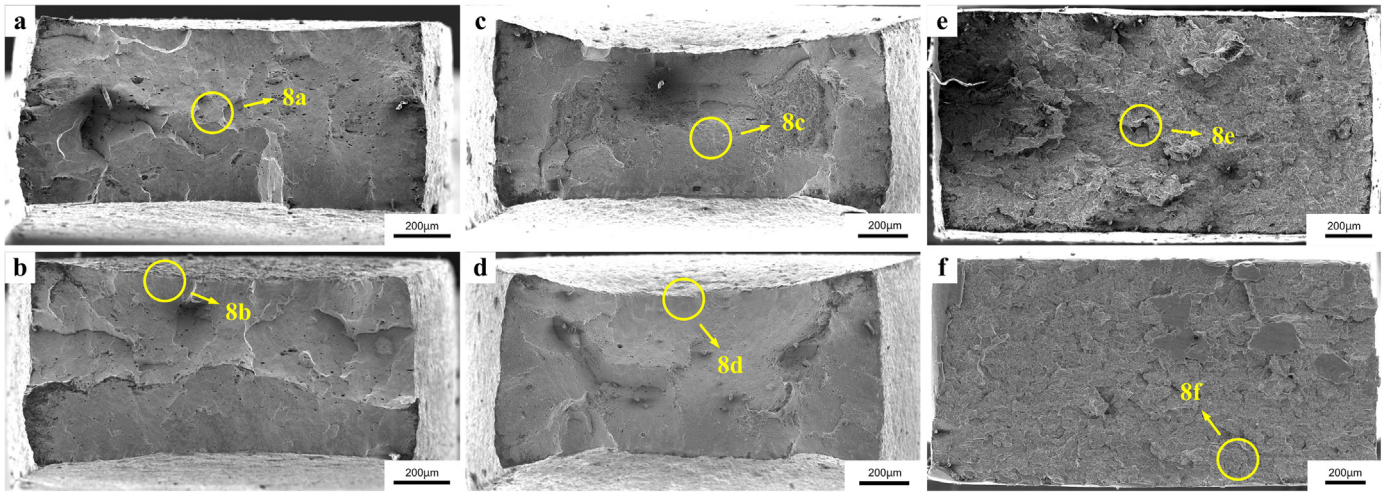

Fig. 7. Fracture morphology of the three materials tested at 77 K with and without hydrogen charging. (a) Uncharged and (b) pre-charged CrMnFeCoNi HEA, (c) uncharged and (d) pre-charged 316L SS and (e) uncharged and (f) pre-charged X80 PS (For interpretation of the references to color in this figure, the reader is referred to the web version of this article.).

$$D_H = D_0 \exp(-\frac{Q - \sigma_h V_H}{RT}) \quad (4)$$

where σ_h is hydrostatic stress, V_H is the partial molar volume of hydrogen, t is the duration of the tensile test. The stress state in our tensile experiment is uniaxial tension so σ_h is estimated to be 600 MPa, which is the average value of the flow stress of the three materials. The average duration t of the tensile tests of the three materials is estimated to be 200 s and we adopt $V_H = 2.0\ cm^3/mol$ from austenitic SS [59] and $V_H = 2.5\ cm^3/mol$ from ferritic steel [60].

Then, we take temperature T to be 300 K, using Eqs. (1) and (4), the diffusion distance L is estimated to be 450 nm for HEA and 316L and 3 mm for X80 at room temperature, respectively. Similarly to the steps above, if we take temperature T to be 77 K, L is estimated to be 3×10^{-11} nm for HEA and 316L and 130 μm for X80 at 77 K, respectively.

The tensile tests and the fracture morphologies above clearly show that the HE resistance of CrMnFeCoNi HEA is higher than the other two materials. For the X80 PS with ferritic structure, it has significantly low resistance to HE both at room temperature and 77 K. Through the estimation of diffusion distances of hydrogen in the tensile test at 77 K for the three materials, we can conclude that the hydrogen diffusion effect is negligible for HEA and 316L, since the diffusion distance (3×10^{-11} nm) is extremely short, while it still works on X80 because the diffusion distance L is 130 μm, which is much larger than the lattice constant of ferrite. Due to larger diffusivity and smaller solubility, it is easier for hydrogen to enter the ferritic steels and diffuse to the stressed or strained areas, which may eventually lead to the formation of internal microcracks such as hydrogen bubbles [17,18,28].

On the other hand, 316L SS is composed of stable austenite which serves as strong traps for hydrogen in the material matrix [24,61],

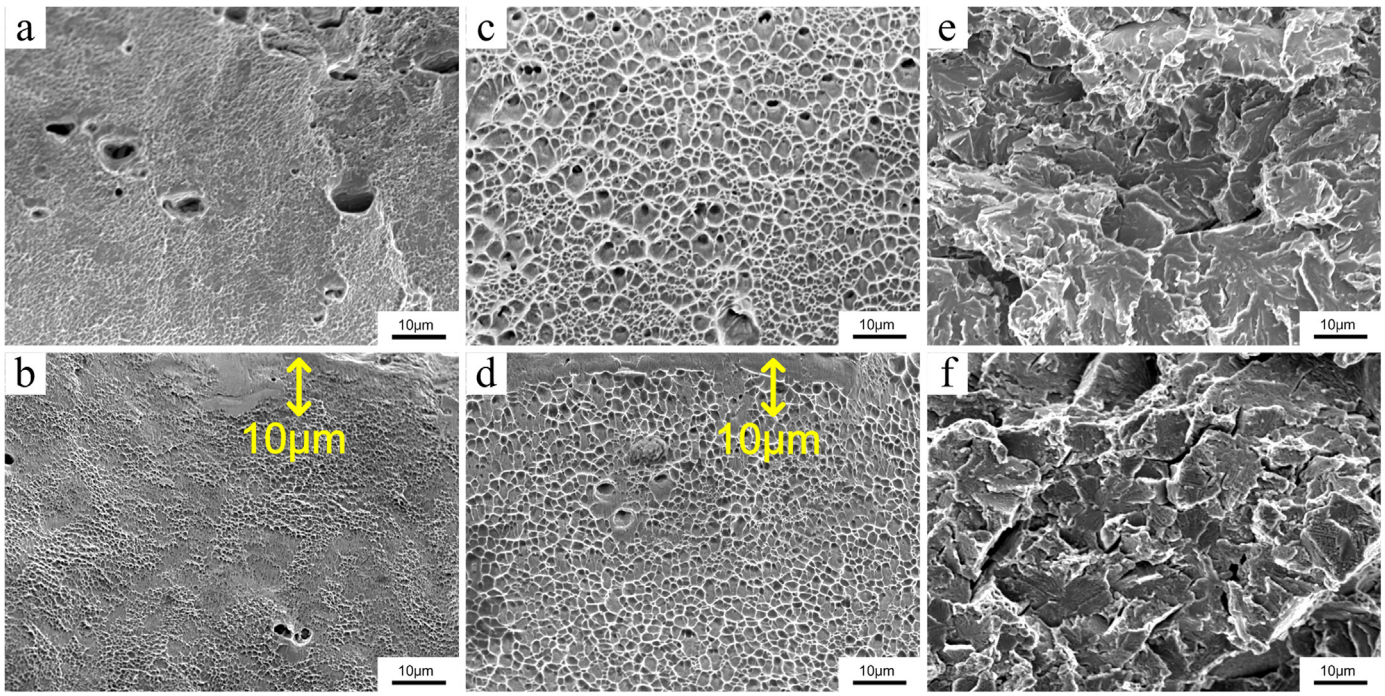

Fig. 8. Typical local area of fracture surfaces of the three materials tested at 77 K with and without hydrogen charging. (a) Uncharged and (b) pre-charged CrMnFeCoNi HEA, (c) uncharged and (d) pre-charged 316L SS and (e) uncharged and (f) pre-charged X80 PS.

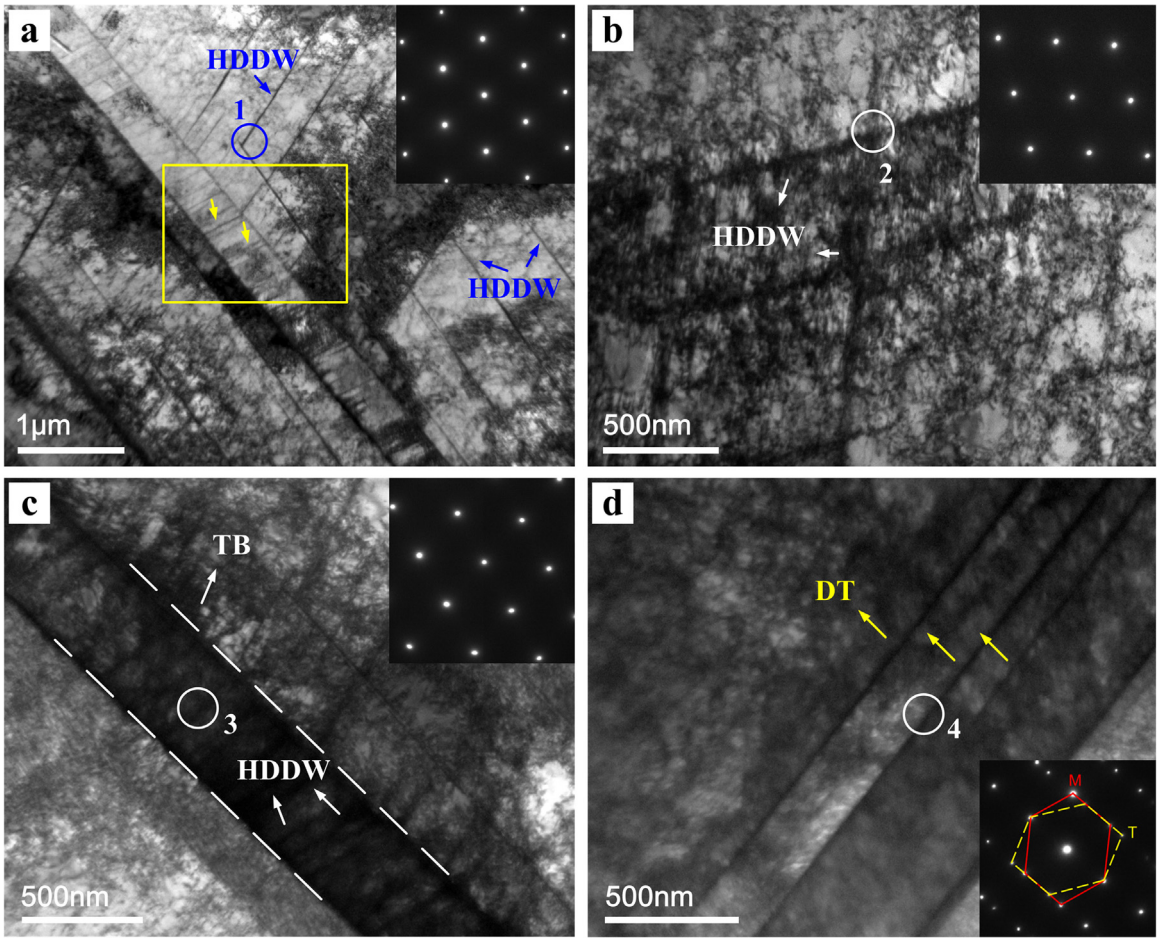

Fig. 9. TEM micrographs of pre-charged 316L SS strained to 15% at room temperature: (a) and (b) tangled dislocations and staggerly distributed HDDWs, (c) a magnified image of the region marked by yellow rectangle in (a), (d) deformation twins and corresponding SAD pattern (For interpretation of the references to color in this figure legend, the reader is referred to the web version of this article.).

resulting in excellent resistance to HE compared with other metallic materials [30,62,63]. However, the factors that control HE are not only crystal structure, diffusivity or solubility, it is also of great importance to consider the deformation mechanisms and the consequent microstructures of the materials during the tensile process [30,33]. Since the CrMnFeCoNi HEA has a better ability to resist HE than 316L, a traditionally good austenite SS with strong HE resistance [30], more details need to be find to reveal why this type of HEA performs so well under hydrogenation conditions.

3.5. Deformation microstructures

Fig. 9 shows micrographs of pre-charged 316L SS strained to 15% at room temperature. The microstructures are substantially nonuniform. One of the characteristics described by Fig. 9a and b is that there are high-density dislocations and many staggered streaks, marked by the blue and white arrows. The insets of the two micrographs show the selected area diffraction (zone 1 and zone 2) where two streaks intersect each other. The streaks are highly dense dislocation walls (HDDWs), since the SAD patterns only reveal one set of diffraction spots with slightly elongated bright lines in the directions perpendicular to the streaks. HDDWs consist of fine dislocation structures or short stacking faults, similar to the structures observed in some other steels [31,64]. The intersections of these HDDWs provide not only high stress fields but also local strain zones that favor to attract hydrogen [33,43]. As a result, the hydrogen trapping sites produced by such intersections will inevitably cause hydrogen localization, when the local hydrogen concentration exceeds a threshold level, the mechanism that causes HE will be triggered.

Fig. 9c shows the magnified image of the region highlighted by the yellow rectangle in Fig. 9a, where there is an annealing twin with long straight twin boundaries (TBs). Parallel arrangement of smaller HDDWs (marked by white arrows in Fig. 9c) is formed in the grain, leading to many intersections of HDDWs and the TBs. Similar to the HDDW-HDDW intersections in Fig. 9a and b, the HDDW-TB intersections also provide many sites for the accumulation of hydrogen because high stress concentration can be produced here.

Fig. 9d shows the deformation twins (DTs) surrounded by high-density dislocations. The corresponding SAD pattern (zone 4) reveals two sets of diffraction spots which belong to FCC deformation twin and matrix (see the inset in Fig. 9d). During deformation, the dislocations will intersect the TBs through a dislocation dissociation mechanism [65,66]. By forming partial dislocations such as $\frac{1}{6}$[211], the coherency of TBs is weakened by the dislocation-twin interactions [67]. As a consequence, highly strained fields that promote hydrogen accumulation are created on the twin boundaries.

Fig. 10 presents typical deformation microstructures for the pre-charged CrMnFeCoNi HEA specimen strained to 15% at room temperature, which are substantially different from 316L SS. It is noticed that highly dense dislocations scatter all over the grains but no obvious HDDWs appear. Fig. 10b and c are magnified micrographs to show these highly tangled dislocations structures, which will not cause prominent strain localization compared to some other planar lattice defects such as stacking faults or ε-martensites [30]. Similarly, in comparison

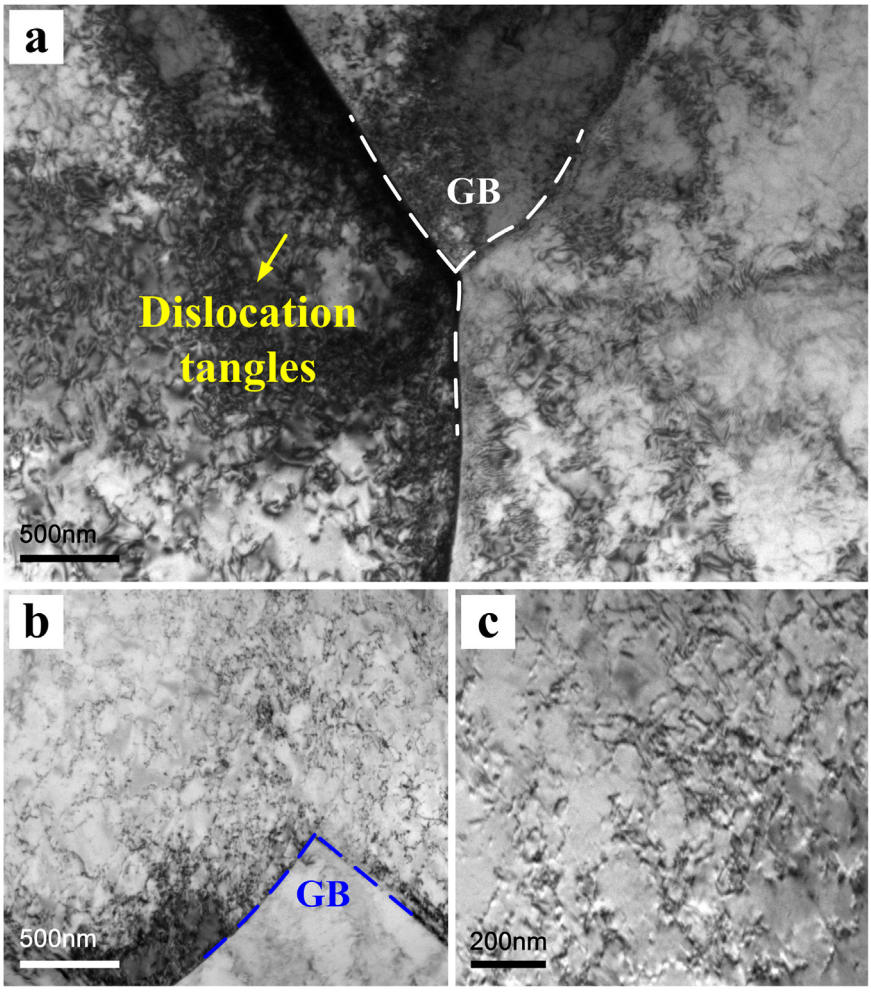

Fig. 10. TEM micrographs of pre-charged CrMnFeCoNi HEA strained to 15% at room temperature: (a) high dense dislocations scattering all over the grains, (b) and (c) magnified micrographs showing the tangled dislocation structures (For interpretation of the references to color in this figure, the reader is referred to the web version of this article.).

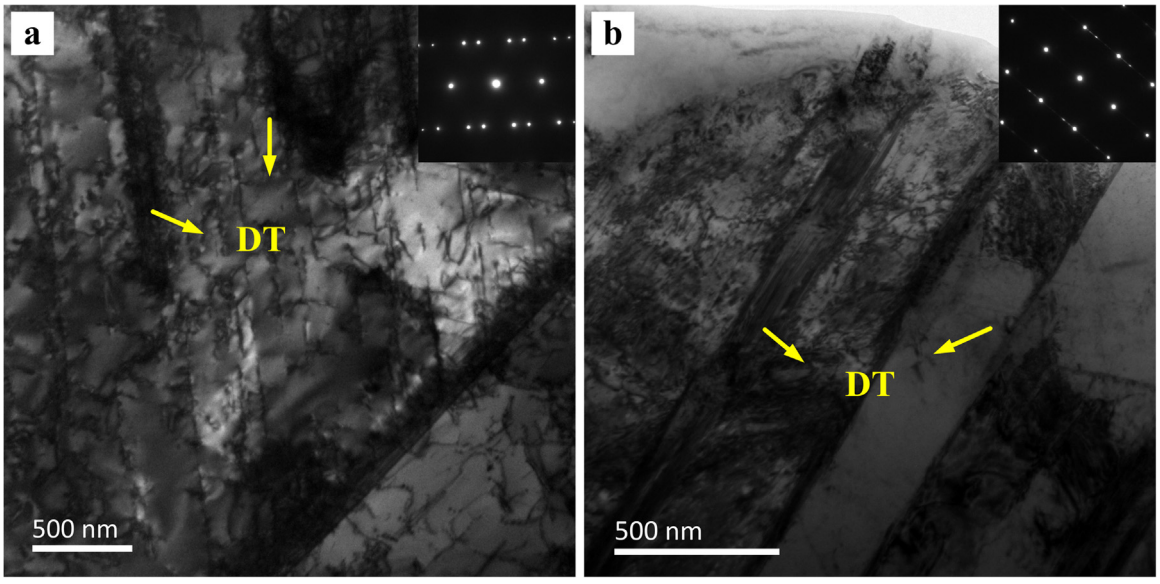

Fig. 11. TEM micrographs of pre-charged: (a) CrMnFeCoNi HEA and (b) 316L SS strained to 15% at 77 K.

with the HDDWs formed in 316L SS that will lead to relatively large strain localization, the tangled dislocations in CrMnFeCoNi HEA only cause lower degree of strain localization. The relatively lower strain localization leads to a lower degree of hydrogen accumulation at the tangled dislocations, so the cracks do not form easily there. Thus, relatively smaller degree of HE is found in CrMnFeCoNi HEA.

Fig. 11 shows the micrographs of pre-charged CrMnFeCoNi HEA (Fig. 11a) and 316L SS (Fig. 11b) strained to 15% at 77 K. Different from the result at room temperature (Fig. 9 and Fig. 10), there are more deformation twin bands in both materials (marked by the yellow arrows), which is the result of increased flow stress at cryogenic temperature [68]. It is reasonable to speculate that the number of hydrogen trap sites produced by TBs and twin-dislocation interactions are more at 77 K than that at room temperature, thus a lower ability to resist HE is displayed at 77 K. However, for the both materials, the HE resistance are higher at 77 K than that at room temperature (see Fig. 3a, b and Fig. 4a, b). A common explanation for the almost zero HE susceptibility of CrMnFeCoNi HEA and 316L SS at 77 K is that when the experimental temperature is extremely low, even if slowly strained, the atomic hydrogen in the materials is unable to get enriched by diffusing to the stress or strain concentration sites within the test process [49,57].

3.6. Hydrogen-enhanced localized plasticity (HELP)

The study on the deformation microstructure only explains HE from the point of hydrogen trapping and accumulation, however, more specific mechanisms that lead to crack initiation by hydrogen in the HE problem need to be revealed. From the discussion above, it is reasonable to speculate that the local hydrogen content in both the CrMnFeCoNi HEA and 316L SS is getting higher and higher during the deformation process, once it exceeds the threshold level, the mechanisms that lead to crack initiation are triggered. In this study, the HELP mechanism is considered to be significant since it is more prominent in materials that are prone to planer slip [45], which is found in both CrMnFeCoNi HEA [5] and 316L SS [69].

According to the HELP mechanism, hydrogen will enhance the movement of dislocation in one direction by reducing the interactions with its elastic centers [20,36]. As a consequence, cross-slip of materials is hindered, which finally leads to localized deformation such as slip planarity [37]. By comparison of the micrographs of Fig. 9 and Fig. 10, we can see that a lot of long straight HDDWs form during the deformation of 316L SS while almost no HDDW is observed in CrMnFeCoNi HEA at the same strain stage. As fine dislocation structures, HDDWs are known to be one of the results of slip planarity [31,64]. Therefore, hydrogen will aggravate the degree of the planar slip which is high enough in the uncharged 316L SS in compare with CrMnFeCoNi HEA. Furthermore, the HDDWs, the HDDW-HDDW intersections, and the HDDW-TB intersections will be potential obstacles which increase the degree of dislocation pile-ups. As a result, high stress concentration is produced and microvoids will nucleate in the vicinity of these dislocation pile-ups.

On the other hand, despite that the solute hydrogen can enhance the mobility of dislocations, which allows them to multiply or move at reduced stresses [36], this effect of hydrogen on the dislocations in HEA will be somehow weakened. Since one of the four core effects of HEA is severe lattice distortion which offers resistance to dislocation motion [1,48], the mobility of dislocations in HEA may not be enhanced as high as that of traditional steels at the same hydrogen concentration. Hence, in the present CrMnFeCoNi HEA case, the effect of the hydrogen on the motion of dislocations is relatively small compared with 316L SS. Localized deformation is thereby more difficult to happen in CrMnFeCoNi HEA, leading to a higher HE resistance.

4. Conclusions

The effect of hydrogen on tensile ductility of CrMnFeCoNi HEA, 316L SS and X80 PS at both room and cryogenic temperature are studied in this work. The HE resistance of the first two materials are examined in details since they have the same crystal structures and prominently better abilities to resist HE than X80 PS. Accordingly, the following conclusions can be drawn:

(1) At room temperature, the HE susceptibility of CrMnFeCoNi HEA, 316L SS and X80 PS are 13%, 25% and 53%, respectively, suggesting that the CrMnFeCoNi HEA has the highest HE resistance.
(2) At 77 K, due to lower diffusivity of hydrogen, tensile ductility of CrMnFeCoNi HEA and 316L SS are almost unaffected by hydrogen while the elongation of pre-charged X80 PS is still reduced.
(3) The fractographs of hydrogen uncharged and pre-charged CrMnFeCoNi HEA and 316L SS exhibit slight difference at both 293 K and 77 K, which are mainly composed of dimples. In contrast, quasi-cleavage features are shown in the fracture surfaces of the pre-charged X80 PS at both 293 K and 77 K.
(4) At room temperature, the deformation of CrMnFeCoNi HEA is mainly accommodated by tangled dislocations while that of 316L SS is dominated by HDDWs. HDDWs are the result of slip planarity and provide the hydrogen trapping sites. Less hydrogen trapping sites and lower degree of hydrogen enrichment in CrMnFeCoNi HEA lead to a better ability to resist HE according to HELP mechanism. At 77 K, more deformation twins are formed in the both materials. A very slow diffusion rate of atomic hydrogen at this temperature prevents hydrogen from an effective enrichment, and therefore has minor effect on the ductility of these two materials.

Acknowledgement

This work is financially supported by the National Key Research and Development Program of China (No. 2017YFB0702003), the NSFC (No. 11472287, No. 11790292, and No. 11572324), the Strategic Priority Research Program of the Chinese Academy of Sciences (Grant Nos. XDB22040302 and XDB22040303), and the Key Research Program of Frontier Sciences (Grant No. QYZDJSSW-JSC011).

References

[1] Y. Zhang, T.T. Zuo, Z. Tang, M.C. Gao, K.A. Dahmen, P.K. Liaw, Z.P. Lu, Microstructures and properties of high-entropy alloys, Prog. Mater. Sci. 61 (2014) 1–93, https://doi.org/10.1016/j.pmatsci.2013.10.001.
[2] D.B. Miracle, O.N. Senkov, A critical review of high entropy alloys and related concepts, Acta Mater. 122 (2017) 448–511, https://doi.org/10.1016/j.actamat.2016.08.081.
[3] J.W. Yeh, S.K. Chen, S.J. Lin, J.Y. Gan, T.S. Chin, T.T. Shun, C.H. Tsau, S.Y. Chang, Nanostructured high-entropy alloys with multiple principal elements: Novel alloy design concepts and outcomes (+274), Adv. Eng. Mater. 6 (2004) 299–303, https://doi.org/10.1002/adem.200300567.
[4] B. Cantor, I.T.H. Chang, P. Knight, A.J.B. Vincent, Microstructural development in equiatomic multicomponent alloys, Mater. Sci. Eng. A 375–377 (2004) 213–218, https://doi.org/10.1016/j.msea.2003.10.257.
[5] F. Otto, A. Dlouhý, C. Somsen, H. Bei, G. Eggeler, E.P. George, The influences of temperature and microstructure on the tensile properties of a CoCrFeMnNi high-entropy alloy, Acta Mater. 61 (2013) 5743–5755, https://doi.org/10.1016/j.actamat.2013.06.018.
[6] Z. Li, K.G. Pradeep, Y. Deng, D. Raabe, C.C. Tasan, Metastable high-entropy dual-phase alloys overcome the strength-ductility trade-off, Nature 534 (2016) 227–230, https://doi.org/10.1038/nature17981.
[7] J.Y. He, H. Wang, H.L. Huang, X.D. Xu, M.W. Chen, Y. Wu, X.J. Liu, T.G. Nieh, K. An, Z.P. Lu, A precipitation-hardened high-entropy alloy with outstanding tensile properties, Acta Mater. 102 (2016) 187–196, https://doi.org/10.1016/j.actamat.2015.08.076.
[8] B. Gludovatz, A. Hohenwarter, D. Catoor, E.H. Chang, E.P. George, R.O. Ritchie, A fracture-resistant high-entropy alloy for cryogenic applications, Science (80-.) 345 (2014) 1153–1158, https://doi.org/10.1126/science.1254581.
[9] M.A. Hemphill, T. Yuan, G.Y. Wang, J.W. Yeh, C.W. Tsai, A. Chuang, P.K. Liaw, Fatigue behavior of Al0.5CoCrCuFeNi high entropy alloys, Acta Mater. 60 (2012) 5723–5734, https://doi.org/10.1016/j.actamat.2012.06.046.
[10] X. Li, B. Gong, C. Deng, Y. Li, Failure mechanism transition of hydrogen embrittlement in AISI 304 K-TIG weld metal under tensile loading, Corros. Sci. 130 (2018) 241–251, https://doi.org/10.1016/j.corsci.2017.10.032.
[11] K. Tokunaga, M.J. Baldwin, R.P. Doerner, N. Noda, Y. Kubota, N. Yoshida, T. Sogabe, T. Kato, B. Schedler, Blister formation and deuterium retention on

tungsten exposed to low energy and high flux deuterium plasma, J. Nucl. Mater. 337–339 (2005) 887–891, https://doi.org/10.1016/j.jnucmat.2004.10.137.
[12] T. Zhang, W. Zhao, T. Li, Y. Zhao, Q. Deng, Y. Wang, W. Jiang, Comparison of hydrogen embrittlement susceptibility of three cathodic protected subsea pipeline steels from a point of view of hydrogen permeation, Corros. Sci. (2017) 0–1, https://doi.org/10.1016/j.corsci.2017.11.013.
[13] M. Koyama, C.C. Tasan, E. Akiyama, K. Tsuzaki, D. Raabe, Hydrogen-assisted decohesion and localized plasticity in dual-phase steel, Acta Mater. 70 (2014) 174–187, https://doi.org/10.1016/j.actamat.2014.01.048.
[14] T. Neeraj, R. Srinivasan, J. Li, Hydrogen embrittlement of ferritic steels: observations on deformation microstructure, nanoscale dimples and failure by nanovoiding, Acta Mater. 60 (2012) 5160–5171, https://doi.org/10.1016/j.actamat.2012.06.014.
[15] N. Eliaz, D. Eliezer, Overview of hydrogen interaction with amorphous alloys, Adv. Perform. Mater. 6 (1999) 5–31, https://doi.org/10.1023/A:1008748627295.
[16] O. Verners, G. Psofogiannakis, A.C.T. van Duin, Comparative molecular dynamics study of fcc-Al hydrogen embrittlement, Corros. Sci. 98 (2015) 40–49, https://doi.org/10.1016/j.corsci.2015.05.008.
[17] J.B. Condon, T. Schober, Hydrogen bubbles in metals, J. Nucl. Mater. 207 (1993) 1–24, https://doi.org/10.1016/0022-3115(93)90244-S.
[18] H.C. Rogers, Hydrogen Embrittlement of Meta, Hydrogen Embrittlement of Metals 159 (1968) 1057–1064, https://doi.org/10.1126/science.159.3819.1057.
[19] W.H. Johnson, On some remarkable changes produced in iron and steel by the action of hydrogen and acids, Proc. R. Soc. Lond. 23 (1874) 168–179, https://doi.org/10.1098/rspl.1874.0024.
[20] P.J. Ferreira, I.M. Robertson, H.K. Birnbaum, Hydrogen effects on the interaction between dislocations, Acta Mater. 46 (1998) 1749–1757, https://doi.org/10.1016/S1359-6454(97)00349-2.
[21] M. Dadfarnia, A. Nagao, S. Wang, M.L. Martin, B.P. Somerday, P. Sofronis, Recent advances on hydrogen embrittlement of structural materials, Int. J. Fract. 196 (2015) 223–243, https://doi.org/10.1007/s10704-015-0068-4.
[22] D.G. Xie, Z.J. Wang, J. Sun, J. Li, E. Ma, Z.W. Shan, In situ study of the initiation of hydrogen bubbles at the aluminium metal/oxide interface, Nat. Mater. 14 (2015) 899–903, https://doi.org/10.1038/nmat4336.
[23] H. Vehoff, H.K. Klameth, Hydrogen embrittlement and trapping at crack tips in Ni-single crystals, Acta Metall. 33 (1985) 955–962, https://doi.org/10.1016/0001-6160(85)90189-0.
[24] L.W. Tsay, M.Y. Chi, Y.F. Wu, J.K. Wu, D.Y. Lin, Hydrogen embrittlement susceptibility and permeability of two ultra-high strength steels, Corros. Sci. 48 (2006) 1926–1938, https://doi.org/10.1016/j.corsci.2005.05.042.
[25] J.P. Hirth, Effects of hydrogen on the properties of iron and steel, Metall. Trans. A 11 (1980) 861–890, https://doi.org/10.1007/BF02654700.
[26] I. Moro, L. Briottet, P. Lemoine, E. Andrieu, C. Blanc, G. Odemer, Hydrogen embrittlement susceptibility of a high strength steel X80, Mater. Sci. Eng. A 527 (2010) 7252–7260, https://doi.org/10.1016/j.msea.2010.07.027.
[27] R.P. Gangloff Critical issues in hydrogen assisted cracking of structural alloys Environment-Induced Cracking of Materials 2008 141 165 doi: 10.1016/B978-008044635-6.50015-7.
[28] M.R. Louthan, Hydrogen embrittlement of metals: a primer for the failure analyst, J. Fail. Anal. Prev. 8 (2008) 289–307, https://doi.org/10.1007/s11668-008-9133-x.
[29] T. Michler, C. San Marchi, J. Naumann, S. Weber, M. Martin, Hydrogen environment embrittlement of stable austenitic steels, Int. J. Hydrog. Energy 37 (2012) 16231–16246, https://doi.org/10.1016/j.ijhydene.2012.08.071.
[30] M. Hatano, M. Fujinami, K. Arai, H. Fujii, M. Nagumo, Hydrogen embrittlement of austenitic stainless steels revealed by deformation microstructures and strain-induced creation of vacancies, Acta Mater. 67 (2014) 342–353, https://doi.org/10.1016/j.actamat.2013.12.039.
[31] H.-S. Noh, J.-H. Kang, K.-M. Kim, S.-J. Kim, The effect of carbon on hydrogen embrittlement in stable Cr-Ni-Mn-N austenitic stainless steels, Corros. Sci. 124 (2017) 63–70, https://doi.org/10.1016/j.corsci.2017.05.004.
[32] F. Galliano, E. Andrieu, C. Blanc, J.M. Cloue, D. Connetable, G. Odemer, Effect of trapping and temperature on the hydrogen embrittlement susceptibility of alloy 718, Mater. Sci. Eng. A 611 (2014) 370–382, https://doi.org/10.1016/j.msea.2014.06.015.
[33] M. Koyama, E. Akiyama, K. Tsuzaki, D. Raabe, Hydrogen-assisted failure in a twinning-induced plasticity steel studied under in situ hydrogen charging by electron channeling contrast imaging, Acta Mater. 61 (2013) 4607–4618, https://doi.org/10.1016/j.actamat.2013.04.030.
[34] L. Zhang, M. Wen, M. Imade, S. Fukuyama, K. Yokogawa, Effect of nickel equivalent on hydrogen gas embrittlement of austenitic stainless steels based on type 316 at low temperatures, Acta Mater. 56 (2008) 3414–3421, https://doi.org/10.1016/j.actamat.2008.03.022.
[35] J. Yang, Y. Song, Y. Lu, J. Gu, Z. Guo, Effect of ferrite on the hydrogen embrittlement in quenched-partitioned-tempered low carbon steel, Mater. Sci. Eng. A 712 (2018) 630–636, https://doi.org/10.1016/j.msea.2017.12.032.
[36] I.M. Robertson, The effect of hydrogen on dislocation dynamics, Eng. Fract. Mech. 64 (1999) 649–673, https://doi.org/10.1016/S0013-7944(99)00094-6.
[37] P. Rozenak, Hydrogen effects on the behavior of dislocations in austenitic stainless-steel, J. Mater. Sci. Lett. 9 (1990) 627–629, https://doi.org/10.1007/bf00721785.
[38] G. Lu, Q. Zhang, N. Kioussis, E. Kaxiras, Hydrogen-enhanced local plasticity in aluminum: an ab initio study, Phys. Rev. Lett. 87 (2001) 955011–955014, https://doi.org/10.1103/PhysRevLett.87.095501.
[39] P. Sofronis, H.K. Birnbaum, Mechanics of the hydrogen-dislocation-impurity interactions—I. Increasing shear modulus, J. Mech. Phys. Solids 43 (1995) 49–90, https://doi.org/10.1016/0022-5096(94)00056-B.
[40] P. Sofronis, The influence of mobility of dissolved hydrogen on the elastic response of a metal, J. Mech. Phys. Solids 43 (1995) 1385–1407, https://doi.org/10.1016/0022-5096(95)00037-J.
[41] Y. Liang, P. Sofronis, N. Aravas, On the effect of hydrogen on plastic instabilities in metals, Acta Mater. 51 (2003) 2717–2730, https://doi.org/10.1016/S1359-6454(03)00081-8.
[42] K.A. Nibur, B.P. Somerday, D.K. Balch, C. San Marchi, The role of localized deformation in hydrogen-assisted crack propagation in 21Cr-6Ni-9Mn stainless steel, Acta Mater. 57 (2009) 3795–3809, https://doi.org/10.1016/j.actamat.2009.04.027.
[43] M. Koyama, E. Akiyama, T. Sawaguchi, D. Raabe, K. Tsuzaki, Hydrogen-induced cracking at grain and twin boundaries in an Fe-Mn-C austenitic steel, Scr. Mater. 66 (2012) 459–462, https://doi.org/10.1016/j.scriptamat.2011.12.015.
[44] M. Koyama, E. Akiyama, K. Tsuzaki, Effect of hydrogen content on the embrittlement in a Fe-Mn-C twinning-induced plasticity steel, Corros. Sci. 59 (2012) 277–281, https://doi.org/10.1016/j.corsci.2012.03.009.
[45] Y. Zhao, D.H. Lee, M.Y. Seok, J.A. Lee, M.P. Phaniraj, J.Y. Suh, H.Y. Ha, J.Y. Kim, U. Ramamurty, J. il Jang, Resistance of CoCrFeMnNi high-entropy alloy to gaseous hydrogen embrittlement, Scr. Mater. 135 (2017) 54–58, https://doi.org/10.1016/j.scriptamat.2017.03.029.
[46] K.E. Nygren, K.M. Bertsch, S. Wang, H. Bei, A. Nagao, I.M. Robertson, Hydrogen embrittlement in compositionally complex FeNiCoCrMn FCC solid solution alloy, Curr. Opin. Solid State Mater. Sci. 22 (2018) 1–7, https://doi.org/10.1016/j.cossms.2017.11.002.
[47] Y. Zhao, D.H. Lee, W.J. Kim, M.Y. Seok, J.Y. Kim, H.N. Han, J.Y. Suh, U. Ramamurty, J. il Jang, Influence of pre-strain on the gaseous hydrogen embrittlement resistance of a high-entropy alloy, Mater. Sci. Eng. A 718 (2018) 43–47, https://doi.org/10.1016/j.msea.2018.01.107.
[48] Y.J. Kwon, J.W. Won, S.H. Park, J.H. Lee, K.R. Lim, Y.S. Na, C.S. Lee, Ultrahigh-strength CoCrFeMnNi high-entropy alloy wire rod with excellent resistance to hydrogen embrittlement, Mater. Sci. Eng. A 732 (2018) 105–111, https://doi.org/10.1016/j.msea.2018.06.086.
[49] H. Luo, Z. Li, D. Raabe, Hydrogen enhances strength and ductility of an equiatomic high-entropy alloy, Sci. Rep. 7 (2017) 1–7, https://doi.org/10.1038/s41598-017-10774-4.
[50] H. Luo, Z. Li, W. Lu, D. Ponge, D. Raabe, Hydrogen embrittlement of an interstitial equimolar high-entropy alloy, Corros. Sci. 136 (2018) 403–408, https://doi.org/10.1016/j.corsci.2018.03.040.
[51] K. Ichii, M. Koyama, C.C. Tasan, K. Tsuzaki, Comparative study of hydrogen embrittlement in stable and metastable high-entropy alloys, Scr. Mater. 150 (2018) 74–77, https://doi.org/10.1016/j.scriptamat.2018.03.003.
[52] H.S. Noh, J.H. Kang, K.M. Kim, S.J. Kim, The effect of carbon on hydrogen embrittlement in stable Cr-Ni-Mn-N austenitic stainless steels, Corros. Sci. 124 (2017) 63–70, https://doi.org/10.1016/j.corsci.2017.05.004.
[53] Y. Zhao, D.H. Lee, J.A. Lee, W.J. Kim, H.N. Han, U. Ramamurty, J.Y. Suh, J. il Jang, Hydrogen-induced nanohardness variations in a CoCrFeMnNi high-entropy alloy, Int. J. Hydrog. Energy 42 (2017) 12015–12021, https://doi.org/10.1016/j.ijhydene.2017.02.061.
[54] C.S. Marchi, B.P. Somerday, S.L. Robinson, Permeability, solubility and diffusivity of hydrogen isotopes in stainless steels at high gas pressures, Int. J. Hydrog. Energy 32 (2007) 100–116, https://doi.org/10.1016/j.ijhydene.2006.05.008.
[55] Y. Kim, Y. Kim, D. Kim, S. Kim, W. Nam, H. Choe, Effects of hydrogen diffusion on the mechanical properties of austenite 316L steel at ambient temperature, Mater. Trans. 52 (2011) 507–513, https://doi.org/10.2320/matertrans.M2010273.
[56] H.B. Xue, Y.F. Cheng, Hydrogen permeation and electrochemical corrosion behavior of the X80 pipeline steel weld, J. Mater. Eng. Perform. 22 (2013) 170–175, https://doi.org/10.1007/s11665-012-0216-1.
[57] K. Yokoyama, T. Eguchi, K. Asaoka, M. Nagumo, Effect of constituent phase of Ni-Ti shape memory alloy on susceptibility to hydrogen embrittlement, Mater. Sci. Eng. A 374 (2004) 177–183, https://doi.org/10.1016/j.msea.2004.02.029.
[58] T. An, H. Peng, P. Bai, S. Zheng, X. Wen, L. Zhang, Influence of hydrogen pressure on fatigue properties of X80 pipeline steel, Int. J. Hydrog. Energy 42 (2017) 15669–15678, https://doi.org/10.1016/j.ijhydene.2017.05.047.
[59] J.O. Bockris, P. Subramanyan, A thermodynamic analysis of hydrogen in metals in the presence of an applied stress field, Acta Metall. 19 (1971) 1205–1208, https://doi.org/10.1016/0001-6160(71)90053-8.
[60] Q.X. Bai, W.Y. CHU, C.M. Hsiao, Partial molar strain field of hydrogen in Fe, Scr. Metall. 21 (1987) 613–618, https://doi.org/10.1016/0036-9748(87)90370-X.
[61] L.W. Tsay, Y.F. Hu, C. Chen, Embrittlement of T-200 maraging steel in a hydrogen sulfide solution, Corros. Sci. 47 (2005) 965–976, https://doi.org/10.1016/j.corsci.2004.06.017.
[62] A.M. Brass, J. Chêne, Hydrogen uptake in 316L stainless steel: consequences on the tensile properties, Corros. Sci. 48 (2006) 3222–3242, https://doi.org/10.1016/j.corsci.2005.11.004.
[63] C. San Marchi, B.P. Somerday, X. Tang, G.H. Schiroky, Effects of alloy composition and strain hardening on tensile fracture of hydrogen-precharged type 316 stainless steels, Int. J. Hydrog. Energy 33 (2008) 889–904, https://doi.org/10.1016/j.ijhydene.2007.10.046.
[64] I. Gutierrez-Urrutia, D. Raabe, Multistage strain hardening through dislocation substructure and twinning in a high strength and ductile weight-reduced Fe-Mn-Al-C steel, Acta Mater. 60 (2012) 5791–5802, https://doi.org/10.1016/j.actamat.2012.07.018.
[65] S. Mahajan, G.Y. Chin, Formation of deformation twins in F.C.C. crystals, Acta Metall. 21 (1973) 1353–1363, https://doi.org/10.1016/0001-6160(73)90085-0.
[66] L. Rémy, Twin-slip interaction in f.c.c. crystals, Acta Metall. 25 (1977) 711–714, https://doi.org/10.1016/0001-6160(77)90013-X.
[67] Y.B. Wang, M.L. Sui, Atomic-scale in situ observation of lattice dislocations passing

through twin boundaries, Appl. Phys. Lett. 94 (2009) 1–4, https://doi.org/10.1063/1.3072801.

[68] G. Laplanche, A. Kostka, O.M. Horst, G. Eggeler, E.P. George, Microstructure evolution and critical stress for twinning in the CrMnFeCoNi high-entropy alloy, Acta Mater. 118 (2016) 152–163, https://doi.org/10.1016/j.actamat.2016.07.038.

[69] T. Magnin, J.M. Lardon, E. Mines, The influence of a 3.5% NaCl solution on the fatigue damage evolution in a planar slip f.c.c. stainless steel, Mater. Sci. Eng. 76 (1985) 7–10, https://doi.org/10.1016/0025-5416(85)90100-4.